First high-nuclearity mixed-valence polyoxometalate with hierarchical interconnected Zn^{2+} migration channels as an advanced cathode material in aqueous zinc-ion battery

Kai Yang [a,1], Yuanyuan Hu [a,1], Lingyu Li [a], Lulu Cui [a], Lei He [b], Shuanjin Wang [c], Junwei Zhao [a,*], Yu-Fei Song [b,**]

[a] Henan Key Laboratory of Polyoxometalate Chemistry, College of Chemistry and Chemical Engineering, Henan University, Kaifeng, Henan, 475004, China
[b] State Key Laboratory of Chemical Resource Engineering, Beijing University of Chemical Technology, Beijing, 100029, China
[c] The Key Laboratory of Low-carbon Chemistry & Energy Conservation of Guangdong Province, State Key Laboratory of Optoelectronic Materials and Technologies, Sun Yat-sen University, Guangzhou, 510275, China

ABSTRACT

To date, the research on Zn^{2+} storage properties of nanosized high-nuclearity polyoxometalate clusters (HNPCs) in aqueous zinc-ion batteries is still unexplored. Herein, we for the first time utilized the nanosized mixed-valence $K_{10}[V^{IV}_{16}V^{V}_{18}O_{82}]$ (KVO) cluster as a Zn^{2+} storage material to exploit novel Zn/HNPC battery with eminent charge–discharge properties because the 3-D orderly packing of nanosized KVO clusters in the microstructure can engineer and construct multidimensional interconnected Zn^{2+} migration channels, which can endow the KVO host with high electron and Zn^{2+} conductivities and high-efficiency Zn^{2+} migration behavior. As expected, the as-fabricated $Zn/K_{10}[V^{IV}_6V^{V}_{18}O_{82}]$ battery exhibits a high reversible capacity of 401 mAh g^{-1}, good cyclic stability with capacity retention of 93% over 4000 cycles at 3 A g^{-1}, and favorable energy (285 Wh kg^{-1}) and power density (4.5 kW kg^{-1}). A quantitative Zn^{2+} storage mechanism has been proposed based on in-depth insight on Zn^{2+} intercalation/deintercalation behavior and redox reaction process during cycling. This work not only provides a new zinc-ion battery research platform of HNPCs and opens up a new understanding of the Zn^{2+} storage mechanism in the POM host, but also demonstrates a tremendous and promising application potential of HNPCs in aqueous batteries.

1. Introduction

The dominating commercial nonaqueous lithium-ion batteries (LIBs) power human's digital and mobile life on account of their high energy densities. However, increasingly concerned environment, safety and expense issues severely hinder their broad applications in large-scale energy storage systems [1–4]. As alternative candidates, aqueous batteries based on Na^+, K^+, Mg^{2+}, Ca^{2+}, Zn^{2+} and Al^{3+} ions have appealed to considerable interest due to their lower expenses and higher security in contrast to LIBs [4,5]. Among them, zinc-ion batteries (ZIBs) have fascinated increasing attention and made some rapid progresses because of high theoretical capacities (820 mAh g^{-1} and 5855 mAh cm^{-3}), low redox potential of Zn^{2+}/Zn (–0.76 V vs. standard hydrogen electrode),

small ionic radius (~0.076 nm for Zn^{2+} and ~0.43 nm for $Zn(H_2O)_6^{2+}$) as well as environment amity [4,6–9]. However, exploring and discovering suitable Zn^{2+} host materials with high energy and power densities still remain a tremendous and ongoing challenge. Some recent results have indicated that simple vanadium oxides can be employed as the Zn^{2+} hosts and display higher theoretical capacities [2,7,8,10,11]. However, the rate performance and cycling sustainability of the Zn/vanadium oxide batteries are still unacceptable on account of the poor electrical conductivity, narrow interlayer spaces and unstable structures of layered vanadium oxides. Thus, controlling microstructure construction and enlarging layer spaces of layered vanadium oxides by the chemical intercalation of various cation pillars may effectively improve the sluggish Zn^{2+} diffusion kinetics and inhibit irreversible structure
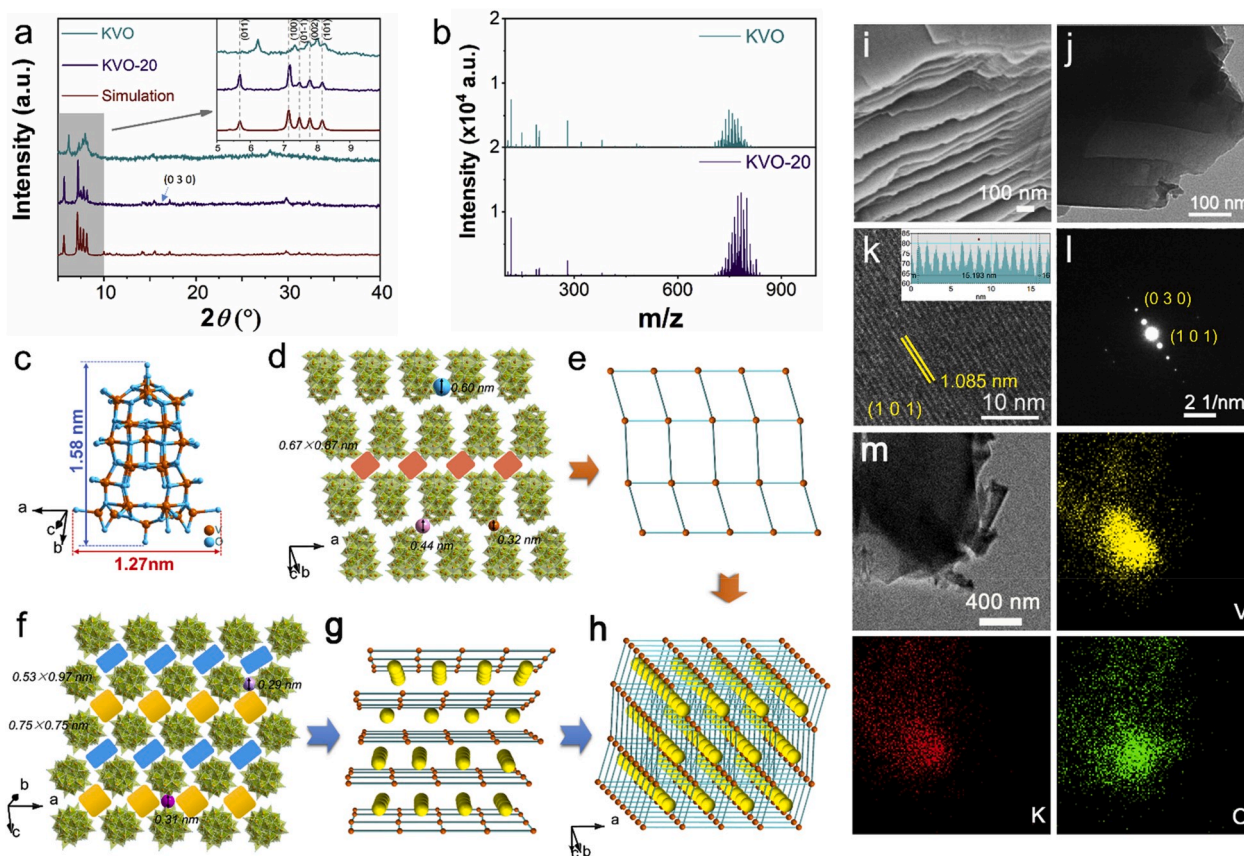
Fig. 1. (a) XRD patterns and (b) ESI–MS spectra of KVO and KVO–20. (c) The molecular structure of the $[V^{IV}_{16}V^{V}_{18}O_{82}]^{10-}$ polyoxoanion in KVO–20. Vanadium: orange, oxygen: blue. (d–e) View of the staggered packing of $[V^{IV}_{16}V^{V}_{18}O_{82}]^{10-}$ along the (0 1–1) face and its topological view in KVO–20. (f) The (0 1 1) face of $[V^{IV}_{16}V^{V}_{18}O_{82}]^{10-}$ arrangement and their Zn^{2+} migration channels highlighted by the rectangles (blue and yellow) and the balls (purple and pink). (g–h) Topologic images of hierarchical interconnected channels based on (0 1–1) face stacked along *b* axis. The continuous yellow balls highlight the migration pathways. (i–l) SEM, TEM, HRTEM and SAED images of KVO–20. (m) TEM image and the corresponding EDS elemental mapping of V, K and O.

destruction [12–16]. Although tremendous efforts have been made to develop outstanding vanadium oxide cathode materials *via* various strategies, the Zn^{2+} diffusion is very limited due to the simplicity of pathways and small size of channels for Zn^{2+} migration and diffusion within layered vanadium oxides and the limited structure regulation ability of simple vanadium oxides derived from too small molecular building blocks. If multidimensional interconnected migration channels can be constructed in the high-nuclear polyoxovanadate cluster (HNPC) host materials, the Zn^{2+} diffusion kinetics would be significantly enhanced. It has been demonstrated that the well-ordered packing of the nanoscaled polyoxometalate (POM) clusters can create the multidimensional interconnected migration channels [17,18], which may meet requirements of fast Zn^{2+} diffusion in aqueous ZIBs. To the best of our knowledge, in-depth investigations on POM-based aqueous ZIBs have not been made to date.

POMs, as a large class of anionic metal-oxygen clusters formed by the condensation of metal-oxide polyhedra in the corner-, edge- or face-sharing manners, possess flexible molecular and electronic structures and have shown excellent electrochemical activities in LIBs, sodium-ion batteries and other energy storage systems [19–26]. As an important and remarkable subclass of POMs, polyoxovanadates (POVs) can construct diverse high-nuclearity mixed-valence cluster structures because vanadium bears flexible oxidation states between +2 and + 5 and behaves as exceptionally rich coordination chemistry under controllable reaction conditions by prudentially varying the pH value, the stoichiometry of reactants, temperature and time in aqueous solution [27]. As a result, POVs display the appealing redox chemistry and can undergo reversible multielectron redox process with keeping the structures unchangable,

leading to a great application potential in the field of energy storage [19–21,23]. Especailly, within the mixed-valence HNPCs, different-valence vanadium centers often inhabit in similar coordination geometries, engender the carried charges to delocalize over the cluster framework and result in faster electron transport and eminent electro-chemical activity [28–33], which can provide a good precondition for the development of aqueous ZIBs. On the other hand, the 3-D packing of large-size molecular HNPCs can construct multidimensional inter-connected migration channels, favoring to the fast Zn^{2+} transport. Thus, we hypothesize that mixed-valence HNPCs may serve as benign Zn^{2+} host materials in ZIBs and effevtively improve the rate performance and cycling sustainability of the Zn/HNPC batteries. As far as we know, there is no report on mixed-valence HNPCs with reversible redox activity and multidimensional interconnected migration packing channels used as the Zn^{2+} host material in aqueous ZIBs.

Under these considerations, in this article, we prepared a nanosized mixed-valence crystalline HNPC $K_{10}[V^{IV}_{16}V^{V}_{18}O_{82}]\cdot20H_2O$ (KVO-20) according to the previous literature [34]. Then, it was dried in a N_2 atmosphere at 200 °C for 3 h to afford $K_{10}[V^{IV}_{16}V^{V}_{18}O_{82}]$ (KVO). The nanosized ellipsoid-shaped $[V^{IV}_{16}V^{V}_{18}O_{82}]^{10-}$ polyoxoanion is con-structed from a central $\{V_4O_8\}$ cube and 30 $\{VO_5\}$ square pyramids through twenty six μ_2-and four μ_3-oxygen atoms. Moreover, the 3-D packing alignment of $[V^{IV}_{16}V^{V}_{18}O_{82}]^{10-}$ polyoxoanions and K^+ cations gives rise to available multidimensional interconnected Zn^{2+} migration channels. As anticipated, the as-fabricated Zn/KVO battery exhibits high energy density (285 Wh kg^{-1}), power density (4.5 kW kg^{-1}) and a considerable long-term cycle performance (4000 cycles at 3 A g^{-1}) with impressive capacity retention (*ca.* 93%). More importantly, the Zn^{2+}
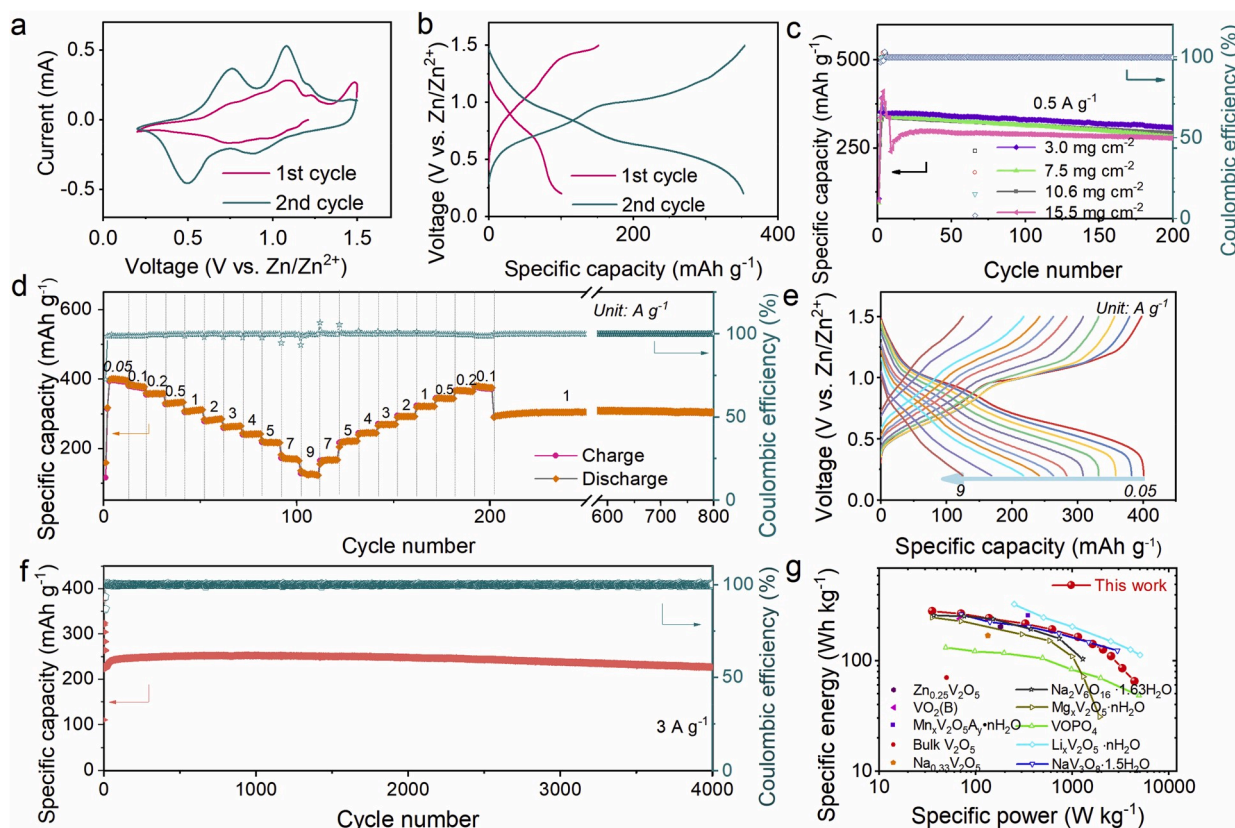
Fig. 2. (a) CV curves and (b) discharge–charge profiles of batteries equipped with KVO cathodes in the first two cycles. (c) Cycle performances of batteries with different areal mass loadings with the KVO cluster at a current density of 0.5 A g^{-1}. (d–e) Rate performance and the discharge–charge profiles of batteries at different current densities. (f) Long-cycle performance of the battery equipped with KVO cathode at 3 A g^{-1}. (g) Ragone plots: comparison of energy and power densities of the Zn/KVO battery with ZIBs based on other reported cathodes.

storage mechanism and redox reversibility of KVO in the electrochemical process were systematically investigated and elucidated. This finding not only opens up a promising platform of HNPCs applied to the ZIB field, but also displays a great potential of HNPCs in the field of new energy batteries.

2. Results and discussion

The crystalline $K_{10}[V^{IV}_{16}V^{V}_{18}O_{82}]\cdot 20H_2O$ (KVO–20) was synthesized according to the literature (see Supporting Information) [34], and then dried in N_2 at 200 °C for 3 h to remove the water molecules (based on the TGA result, Fig. S1), giving rise to the final product KVO. As shown in Fig. 1a, the simulated XRD pattern of KVO–20 (CCDC No: 1671647) matches well with the experimental result of KVO–20. It should be pointed out that the slight shifts of (0 1 1), (1 0 0), (0 1–1), (0 0 2) and (1 0 1) diffraction peaks of KVO result from removal of crystal water molecules, leading to the narrow spaces of adjacent HNPC clusters [35]. Electrospray ionization mass spectrometry (ESI–MS) measurements indicate that the polyoxoanion skeleton of the overwhelming majority of $\{V_{34}O_{82}\}$ can still retain unchanged in aqueous solution (Fig. 1b, Figs. S2a–b, Table S1) [33,36,37], which provides a solid foundation for electrochemical studies of KVO used for the Zn^{2+} host cathode material in rechargeable aqueous ZIBs.

The nanosized ellipsoid-shaped $[V^{IV}_{16}V^{V}_{18}O_{82}]^{10-}$ polyoxoanion with the size 1.27 × 1.58 nm in KVO–20 consists of a central $\{V_4O_8\}$ cube and a $\{V_{30}O_{74}\}$ shell built up from 30 $\{VO_5\}$ square pyramids by sharing edges and corners via twenty six μ_2-and four μ_3-oxygen atoms (Fig. 1c). Adjacent $[V^{IV}_{16}V^{V}_{18}O_{82}]^{10-}$ polyoxoanions are interacted by K^+ cations to form the 2D layer along the (0 1–1) plane (Fig. 1d). If taking the $[V^{IV}_{16}V^{V}_{18}O_{82}]^{10-}$ polyoxoanion as a 4-connected node, the 2D layer can be simplified as a (4, 4) topology network (Fig. 1e). The layer packing structures constructed from $[V^{IV}_{16}V^{V}_{18}O_{82}]^{10-}$ polyoxoanions and K^+ cations contain plentiful channels (0.67 × 0.87 nm) and open gaps with three sizes (0.60 nm, 0.44 nm and 0.32 nm) for fast Zn^{2+} diffusion rate (Fig. 1d–h). Combined with the interlayer pathways including two types of channels (0.53 × 0.97 nm and 0.75 × 0.75 nm) and two sizes of gaps among the clusters (0.29 nm and 0.31 nm, Fig. 1f and g), KVO clusters construct hierarchical interconnected migration channels in different spatial dimensions to improve the Zn^{2+} transport capacity (Fig. S3a). The uniform continuous spatial 2D layer structure built by $[V^{IV}_{16}V^{V}_{18}O_{82}]^{10-}$ polyoxoanions and K^+ cations can also be observed in SEM and TEM morphologies (Fig. 1i and j), which is beneficial for the Zn^{2+} migration. Furthermore, the measured lattice spacing of 1.085 nm in the high-resolution TEM (HRTEM) image agrees well with the arrangement of $[V^{IV}_{16}V^{V}_{18}O_{82}]^{10-}$ polyoxoanions in the (1 0 1) face (Fig. 1k, Fig. S3b). The selected area electron diffraction (SAED) image verifies its single-crystal nature, which corresponds to the XRD result. The observed HRTEM image of (0 1–1) face further confirms the crystalline structure feature of KVO–20 (Figs. S3c–e). TEM and SEM morphologies and elemental mapping images demonstrate the layered structure of KVO and homogeneous distribution of K, V and O atoms (Fig. 1k, Fig. S4). Inductively coupled plasma atom emission spectroscopy (ICP–AES) can quantify the stoichiometric ratio of K and V in KVO (Table S2). Moreover, the electric conductivities of KVO–20, KVO and V_2O_5 have been measured by an in-situ micro-four-point probe technique under low pressures (0.5, 1.0, 2.0, 4.0 MPa) at room temperature (Fig. S5). Experimental results exhibit that the electrical conductivities of KVO–20, KVO and V_2O_5 respectively vary in 2.15×10^{-5} – 2.71×10^{-5} S cm^{-1}, 2.30×10^{-5} – 2.79×10^{-5} S cm^{-1} and 0.77×10^{-5} – 1.4×10^{-5} S cm^{-1} under low pressures of 0.5, 1.0, 2.0, 4.0 MPa. It can been
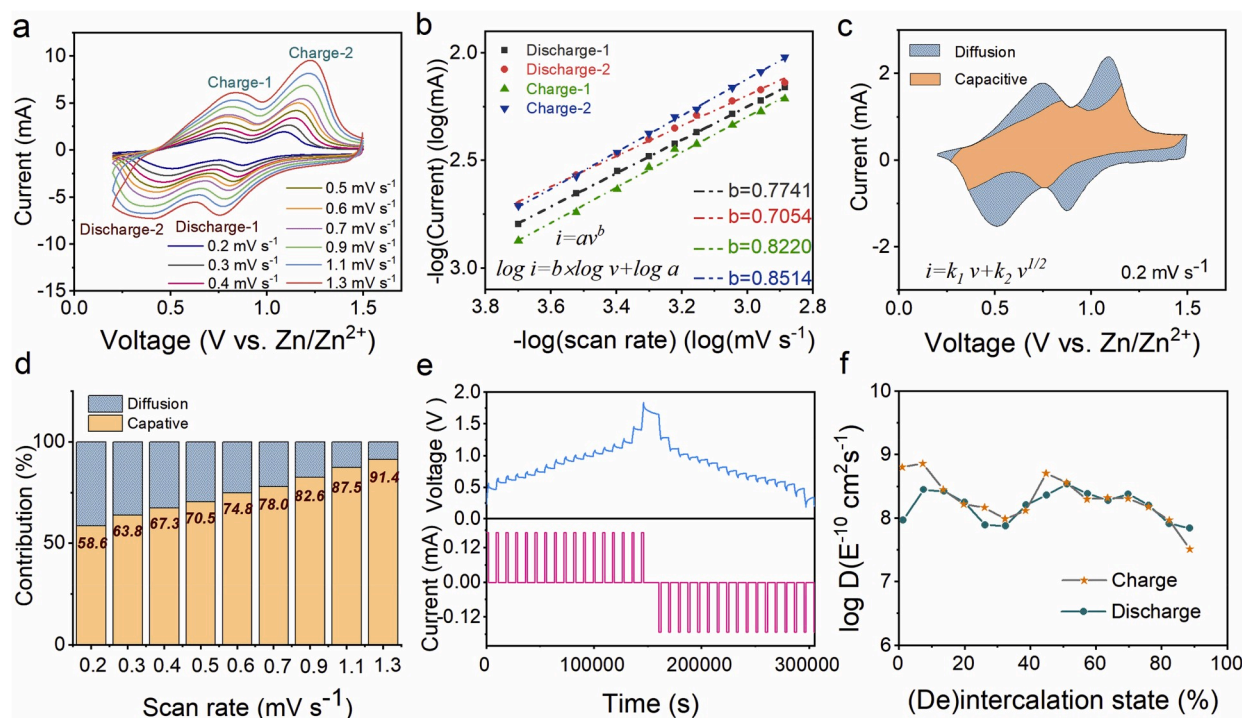
Fig. 3. (a) CV curves of the KVO cathode at different scan rates. (b) –log(current) vs. –log(scan rate) plots of four peaks in the CV curves during cycling. (c) Pseudocapacitive fraction (shown by the orange area) calculated at a scan rate of 0.2 mV s^{-1} from CV curves at different scan rates and (d) pseudocapacitive fractions at different scan rates; (e–f) Charge–discharge profiles and time variation of GITT measurement and the corresponding diffusivity coefficients of Zn^{2+} during the charging and discharging processes.

clearly seen that the electrical conductivity of KVO–20 and KVO is better than that of V$_2$O$_5$ under the same conditions (Fig. S5). The as-obtained results can favor to verify the superiority of mixed-valence POVs in electron transport behavior.

To probe its application in ZIBs, we assembled the Zn/HNPC cells using the as-prepared KVO cathode, the Zn foil as the anode and 2.5 M Zn(CF$_3$SO$_3$)$_2$ aqueous solution as the electrolyte. As illustrated by XRD patterns of the KVO cathode in fresh cell and KVO–20 (Fig. S6), the re-hydration effects of dehydrated KVO in aqueous electrolyte can be confirmed. Moreover, the similar electrochemical behaviors of KVO–20 and KVO cathodes during cycling demonstrate that the removal of crystal water molecules could help to afford an accurate quantification of clusters during cathode preparing process, which have no effect on the structural stability of {V$_{30}$O$_{74}$} clusters and Zn^{2+} intercalation/deintercalation behavior, indicating the same Zn^{2+} storage mechanism of KVO–20 and KVO cathodes in Zn/HNPC cells.

Fig. 2a shows the cyclic voltammetry (CV) curves of the first two cycles at the scan rate of 0.1 mV s^{-1} in the voltage window of 0.2–1.5 V. The obvious difference between the oxide peak in the range of 1.4–1.5 V in the first cycle and that in the second cycle during the charging process indicates the discrepant oxidation reactions and the appearance of irreversible oxidative products in the charging process of the first cycle [1,35]. This observation can be proved by varying the charge platform between 1.4 and 1.5 V in the first two galvanostatic charge-discharge (GCD) curves (Fig. 2b). Moreover, the *ex-situ* XRD result at the full charged state(1.5 V) in the first cycle (Fig. S6) further demonstrates the appearance of the oxidative product K$_2$V$_6$O$_{16}$·1.5H$_2$O (JCPDS Card No. 51–0379, to be discussed below).

In this work, the KVO cathode (the areal mass loading: ~3.0 mg cm^{-2}) was used to evaluate specific capacity, capacity retention, cycle stability and rate capability of KVO (Fig. 2 and Fig. S7). It can be seen from Fig. 2c and Fig. S8 that the cathode with the KVO loading of 3.0 mg cm^{-2} delivers 350 mAh g^{-1} capacity with coulombic efficiency around 99% at a current density of 0.5 A g^{-1}, in which a capacity retention of

88.8% is obtained during 200 cycles. The cathode with a high KVO loading of 15.5 mg cm^{-2} exhibits a reversible capacity of 411 mAh g^{-1} at 0.05 A g^{-1}. Granting to the total two-electron transfer between V^{5+} and V^{3+}, we calculated that the theoretical specific capacity of 531 mAh g^{-1} can provide 68 electrons to pass through during the redox reaction according to the equation of theoretical specific capacity ($Q = nF/3.6Mw$). Here, the obtained reversible capacity of 411 mAh g^{-1} at 0.05 A g^{-1} signifies the transfer process of 55 electrons during cycles, revealing a high redox reaction efficiency in the KVO cathode [33]. When tested at the current density of 0.5 A g^{-1}, the high loading cathode presents a stable discharge capacity of 299 mAh g^{-1} with the capacity retention of 93.3% over 200 cycles. Apparently, the better capacity retention of high KVO loading electrode than the low KVO loading cathode can be attributed to the less loss ratio of KVO in solubility equilibrium in the same electrolyte dosage in a single cell [38]. The tardy capacity decay at 0.5 A g^{-1} is ascribed to the dissolution of KVO in water, leading to the loss of active material, which is similar to the capacity decay of lithium-sulfur battery system related to the resolvable sulfur and poly-sulfides [39–41]. Additionally, the occurence of K and V atoms in the ICP–AES results of electrolyte after 2 cycles and 20 cycles indicates the correlation of capacity decay and active material dissolution (Table S2). The capacity decay can be facilely controlled by adjusting the ratio of the electrolyte dosage to the mass of active material (E/A, μL mg^{-1}) in one cell [42,43]. The results in Fig. S9 show that the Zn/KVO battery exhibits better capacity retention (96.6%) when E/A is controlled at 23.3 μL mg^{-1}. In the following discussion, all electrochemical mea-surements are performed at the uniform E/A value (23.3 μL mg^{-1}) to evaluate the properties of the KVO cathode. Apart from the high ca-pacity retention, the Zn/KVO battery also exhibits favorable rate ca-pacity and cycle performance (Fig. 2d–e). When the current density varies from 0.1 to 9 A g^{-1}, the capacity decreases from 383 to 138 mAh g^{-1}. Upon switching back to 0.1 A g^{-1} after 190 cycles, the specific capacity recovers to 380 mAh g^{-1}, revealing excellent recovery capa-bility. After the rate performance test, the Zn/KVO battery still

maintains a capacity of 294 mAh g^{-1} at 1 A g^{-1} with a superior capacity retention as well as cyclic stability over 600 cycles. The excellent rate capability provides the direct evidence of the fast Zn^{2+} diffusion kinetics in the hierarchical interconnected migration channels and unimpeded electron transport in the cathode, which is also proved by electro-chemical impedance spectroscopy (EIS) measurements (Fig. S10). Compared with the fresh cell, the significant decrease of charge transfer resistance after recycling implies that the activated process of bulk KVO cathode can enhance the utilization of the active material and decrease the electrode polarization [44,45]. Moreover, the small ohmic resistance (R_b) indicates the fast electron transport behavior in the fabricated conductive framework of the cathode owing to the conductive mixed-valence HNPCs. The increasing of R_b and the appearance of ion diffusion resistance (R_s) in the high-frequency region should be ascribed to the formation of the irreversible product K$_2$V$_6$O$_{16}$·1.5H$_2$O (Fig. S10). The low charge-transfer resistance (R_{ct}) from the Nyquist plot after cycling means the fast Zn^{2+} immigration in the KVO cathode as well. Impressively, the battery equipped with KVO cathode even at 3 A g^{-1} during cycling exhibits the high capacity of 252.9 mAh g^{-1} and still retains 226.3 mAh g^{-1} after 4000 cycles (Fig. 2f), accompanying with the high coulombic efficiency (~99%), which manifests a super-long-term cycling performance, good electrochemical revers-ibility as well as excellent structure stability of KVO clusters and the Zn^{2+} migration channels. As a result, the Zn/KVO battery (Fig. 2g) displays a superior energy density (285 Wh kg^{-1}) and an impressive power density (4.5 kW kg^{-1}) (based on the mass of KVO in the cathode). In comparison, the Ragone plots further demonstrate that the high en-ergy and power densities of the as-prepared Zn/KVO battery outstrip the majority of the reported batteries based on layered vanadium-based hosts such as Na$_2$V$_6$O$_{16}$·1.63H$_2$O [46], Na$_{0.33}$V$_2$O$_5$ [47], Zn$_{0.25}$V$_2$O$_5$ [48], Mg$_x$V$_2$O$_5$·nH$_2$O [22], VO$_2$ (B) [49], Li$_x$V$_2$O$_5$·nH$_2$O [50], NaV$_3$O$_8$·1.5H$_2$O [52], VOPO$_4$ [35] and V$_2$O$_5$ [53]. Besides, the specific capacity, capacity retention and mass loading of the KVO cathode also have displayed apparent advantages as listed in the summary of those reported host materials (Table S3). Additionally, the fully charged cell shows a minor voltage dropping after standing for 7 days (Fig. S11), manifesting an acceptable calendar life, although there is still room for improvement by a dissolution-inhibiting strategy. In short, the mixed-valence KVO cathode with reversible redox activity and good electrical and Zn^{2+} conductivity is a promising candidate for the Zn^{2+} storage.

To explain the excellent electrochemical performance roundly, the electrochemical mechanism for Zn^{2+} storage behavior in the KVO cathode was achieved by a simple CV method to get insight into the diffusion-controlled and the pseudocapacitive-controlled capacities of the Zn/KVO battery [21,22,50,51]. It can be seen from Fig. 3a that CV curves of the KVO cathode show similar shapes at various scan rates from 0.2 to 1.3 mV s^{-1}, indicating the excellent reversibility. According to the CV curves of different scan rates and the power law relationship between scan rate v and current i ($i = av^b$, where the b value is between 0.5 and 1, b = 0.5 for a diffusion-controlled behavior and 1.0 for a surface-controlled capative response), the b values at peaks of discharge -1, 2 and charge -1, 2 are 0.7741, 0.7054 and 0.8220, 0.8514, respectively, indicating the collaborative control process by ion diffu-sion and pseudocapacitive behavior, as presented in Fig. 3b [54]. The quantitative distribution of diffusion and pseudocapacitive contribution can be analyzed by the previous approach developed by Dunn et al. ($i = k_1v + k_2v^{1/2}$, the total current (i) is divided into the capacitive contri-bution (k_1v) and the diffusion-controlled current ($k_2v^{1/2}$), see details in the supporting information) [54,55]. For example, Fig. 3c displays the capacitive contribution of 58.6% at a scan rate of 0.2 mV s^{-1}. The ratios of pseudocapacitive contribution in the total capacity at different scan rates (0.2–1.3 mV s^{-1}) can be summarized in Fig. 3d. The capacitive contribution gradually holds the predominant place with the increase of scan rate, which can support its good rate capability [11,22,50,56]. The
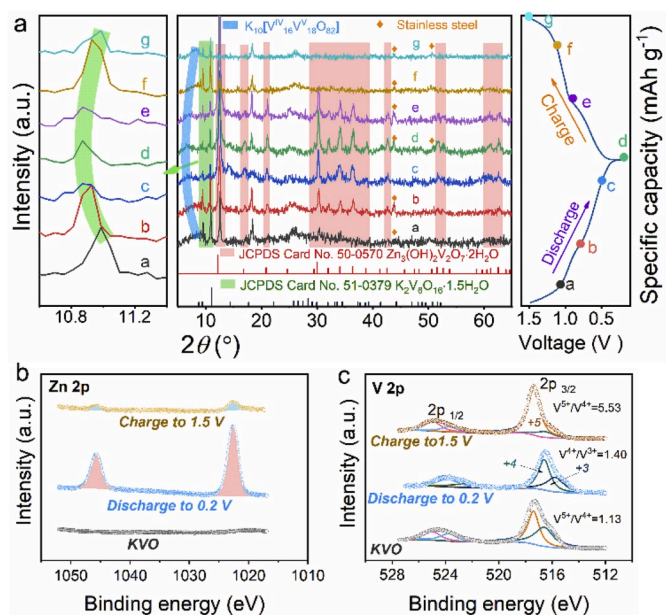

Fig. 4. (a) *Ex-situ* XRD patterns of the KVO cathode at different voltages of the 10th cycle. (b–c) XPS curves for Zn and V elements at different charge/ discharge states of the KVO cathode.

high pseudocapacitive contribution of the KVO cathode can be ascribed to the intercalation pseudocapacitive mechanism [55,57]. In the crys-talline KVO, Zn^{2+} ions can intercalate into the 3D interconnected Zn^{2+} migration channels accompanied by a faradaic charge-transfer with no crystallographic phase change (based on the *ex-situ* XRD patterns in the following part (Fig. 4a and Fig. 4a S6)). Here, crystalline KVO with the engineered 3D interconnected Zn^{2+} migration channels possess abun-dant inner surface and fast Zn^{2+} migration channels in crystalline KVO, which provides vast surface sites and fast diffusion paths to dominate effective redox reactions with vanadium atoms and fast Zn^{2+} diffusion kinetics, increasing capacitive-controlled current espically in high rate. Galvanostatic intermittent titration technique (GITT) that was discussed below substantiates the fast Zn^{2+} diffusion kinetics in the KVO cathode. The nitrogen adsorption–desorption isotherms manifest that the KVO material has a small specific surface (only 1.7 m^2 g^{-1}) (Fig. S12), which can further confirm the intercalation pseudocapacitive mechanism. Therefore, the KVO material may be considered as an intrinsic pseudo-capacitive material exhibiting the characteristics of the capacitive charge storage, which is not affected by particle sizes and morphologies [57]. GITT was employed to lucubrate the Zn^{2+} diffusion kinetics in the KVO cathode (Fig. 3e–f, Fig. S13) [50,58]. Encouragingly, the diffusion coefficient of 10^{-8}–10^{-9} cm^2 s^{-1} for the bulk crystal KVO is higher than those of bulk V$_2$O$_5$ (10^{-10}–10^{-11} cm^2 s^{-1}) [45] and other reported nanoscale layered materials such as layer V$_2$O$_5$ (10^{-9}–10^{-10} cm^2 s^{-1}) [59], nanobelt Zn$_{0.25}$V$_2$O$_5$·nH$_2$O (10^{-9}–10^{-10} cm^2 s^{-1}) [48], porous frameworks Zn$_3$(OH)$_2$V$_2$O$_7$·2H$_2$O (10^{-9}–10^{-10} cm^2 s^{-1}) [11], and VO$_2$ (B) (10^{-11} cm^2 s^{-1}) [60] *etc*. Obviously, although the bulk KVO is directly applied to make the cluster cathode by a simple manual grinding method, the diffusion capability is impressive by virtue of the distinctive hierarchical interconnected Zn^{2+} migration channels.

The phase and structure changes during insertion/extraction of Zn^{2+} ions in the KVO electrode have been elucidated by *ex-situ* XRD and ESI-MS results during the 10th cycle (Fig. 4a). Firstly, the preliminary conclusion of the irreversible product K$_2$V$_6$O$_{16}$·1.5H$_2$O generated in the charging process during the first cycle can be confirmed by XRD patterns (Fig. S6). Accompanied by the formation of the irreversible product, the intensities of KVO peaks [(0 1 1), (1 0 0), (0 1–1), (0 0 2) and (1 0 1)] diminish at the voltage of 1.5 V. Besides, the shift and recovery of characteristic (0 0 2) peak for K$_2$V$_6$O$_{16}$·1.5H$_2$O at 10.9° during the cycle
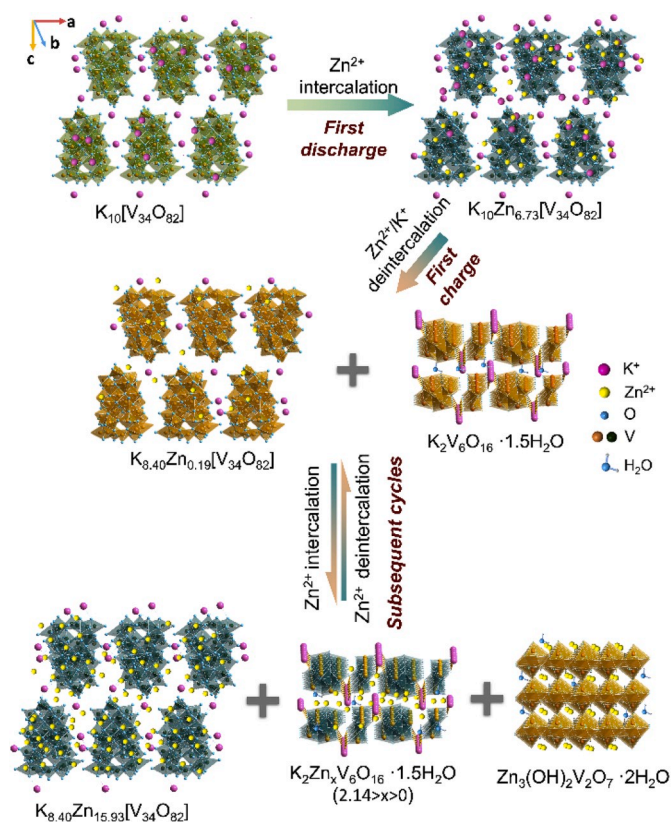
Fig. 5. Schematic illustration of Zn^{2+} intercalation/deintercalation process of the KVO cathode during cycling.

process indicate the reversible Zn^{2+} intercalation/deintercalation behavior in $K_2V_6O_{16} \cdot 1.5H_2O$ as a host material, which is further supported by the studies on the Zn^{2+} storage capability of $K_2V_6O_{16} \cdot 1.5H_2O$ reported by Liang et al. [61]. Secondly, during the discharging process, a new phase of $Zn_3(OH)_2V_2O_7 \cdot 2H_2O$ (JCPDS Card No. 50–0570) appears and increases gradually. Meanwhile, it can be observed that the diffraction intensities of (1 0 0), (0 1–1), (0 0 2) and (1 0 1) peaks decrease in the range of 7.2–8.2° for KVO. During the charging process, $Zn_3(OH)_2V_2O_7 \cdot 2H_2O$ gradually decreases and disappears, suggesting the reversible phase conversion of the $Zn_3(OH)_2V_2O_7 \cdot 2H_2O$ electrode [61, 62]. Furthermore, it can be seen from the blue band marked regions in Fig. 4a that the characteristic KVO peaks of (1 0 0), (0 1–1), (0 0 2) and (1 0 1) in the range of 7.2–8.2° shift toward lower 2θ angles during Zn^{2+} intercalation process and then recover to the original state in the subsequent deintercalation process, suggesting the redox reversibility and structure stability of $[V^{IV}_{16}V^{V}_{18}O_{82}]^{10-}$ clusters. Moreover, TEM and HRTEM images of the KVO cathode after the first and two discharging processes indicate that the crystalline phase of KVO with the enlarged (1 0 1) plane is still maintained during repeated intercalation process, reflecting the stability of the KVO host (Fig. S14). But the lattice information of $K_2V_6O_{16} \cdot 1.5H_2O$ [(3 1 0) and (6 0 0) planes] and $Zn_3(OH)_2$-$V_2O_7 \cdot 2H_2O$ [(0 0 2) plane] can be detected from the second discharge sample, demonstrating the generation of the irreversible products. The detectable polyoxoanion fragments of KVO with charges of −8, −7 and −6 by ESI–MS in KVO cathodes at 0.2 V and 1.5 V further substantiates the redox stability of the cluster in ZIBs (Figs. S2c–d, Table S1) [33].

X-ray photoelectron spectroscopy (XPS) measurement provides an insight into the valence conversion of Zn and V elements during the charging–discharging process (Fig. 4b and c). Compared with the Zn 2p peak of the KVO cathode at initial state, the evident intensity change of Zn 2p peaks at full charge (1.5 V) and discharge (0.2 V) states convincingly proves the effective Zn^{2+} intercalation/deintercalation behavior in the KVO cathode during cycling (Fig. 4b). For the original

KVO cathode, V^{5+} and V^{4+} ions exist. When the battery discharges to 0.2 V, V^{3+} ions can be detected while V^{5+} ions are lost, where V^{5+}/V^{4+} (the molar ratio is 1.125) of KVO converts to V^{4+}/V^{3+} with a molar ratio of 1.40 based on the peak area of XPS, suggesting that the Zn^{2+} guest inserts into the host. After the subsequent charging process, V^{4+}/V^{3+} is oxidized to high-valence V^{5+}/V^{4+} with a molar ratio of 5.53, owing to the almost complete deintercalation of Zn^{2+} ions from the cathode material [63].
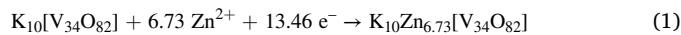
To further uncover a quantitative reaction mechanism in the KVO cathode, the stoichiometric ratios of K, V and Zn elements at different electrochemical states were measured by ICP–AES [47,52]. Since $K_2V_6O_{16} \cdot 1.5H_2O$ and $Zn_3(OH)_2V_2O_7 \cdot 2H_2O$ are insoluble, the stoichiometric ratios of K, V and Zn atoms for the soluble KVO cluster at full charge and discharge states can be calculated from the ICP–AES results (Table S2). After the first charging process, the content decrease of the K element can be ascribed to the formation of irreversible $K_2V_6O_{16} \cdot 1.5H_2O$. Based on the above studies and the reported specific capacity (175 mAh g^{-1} at 0.5 A g^{-1}) of $K_2V_6O_{16} \cdot 1.5H_2O$ in Liang's work [61], we propose a reasonable storage mechanism (Fig. 5).

The detailed electrode reactions are summarized as below:

The first cycle
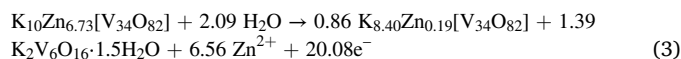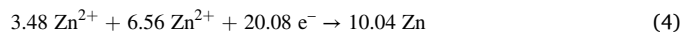
Discharging process:
Cathode:

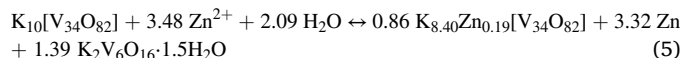$$K_{10}[V_{34}O_{82}] + 6.73\ Zn^{2+} + 13.46\ e^- \rightarrow K_{10}Zn_{6.73}[V_{34}O_{82}] \qquad (1)$$

Anode:

$$6.73\ Zn \rightarrow 6.73\ Zn^{2+} + 13.46\ e^- \qquad (2)$$

Charging process:
Cathode:

$$K_{10}Zn_{6.73}[V_{34}O_{82}] + 2.09\ H_2O \rightarrow 0.86\ K_{8.40}Zn_{0.19}[V_{34}O_{82}] + 1.39\ K_2V_6O_{16} \cdot 1.5H_2O + 6.56\ Zn^{2+} + 20.08\ e^- \qquad (3)$$

Anode:

$$3.48\ Zn^{2+} + 6.56\ Zn^{2+} + 20.08\ e^- \rightarrow 10.04\ Zn \qquad (4)$$

Overall reaction:

$$K_{10}[V_{34}O_{82}] + 3.48\ Zn^{2+} + 2.09\ H_2O \leftrightarrow 0.86\ K_{8.40}Zn_{0.19}[V_{34}O_{82}] + 3.32\ Zn + 1.39\ K_2V_6O_{16} \cdot 1.5H_2O \qquad (5)$$

The subsequently cycles:
Cathode:

$$K_{8.40}Zn_{0.19}[V_{34}O_{82}] + 1.62\ K_2V_6O_{16} \cdot 1.5H_2O + 22.74\ Zn^{2+} + 2y\ H_2O + 45.48\ e^- \leftrightarrow K_{8.40}Zn_{15.93}[V_{34}O_{82}] + yZn_3(OH)_2V_2O_7 \cdot 2H_2O + 1.62\ K_2Zn_xV_6O_{16} \cdot 1.5H_2O\ (2.14 > x > 0,\ 2.33 > y > 1.18) \qquad (6)$$

Anode:

$$22.74\ Zn \leftrightarrow 22.74\ Zn^{2+} + 45.48\ e^- \qquad (7)$$

Overall reaction:

$$K_{8.40}Zn_{0.19}[V_{34}O_{82}] + 1.62\ K_2V_6O_{16} \cdot 1.5H_2O + 2yH_2O + 22.74\ Zn \leftrightarrow K_{8.40}Zn_{15.93}[V_{34}O_{82}] + yZn_3(OH)_2V_2O_7 \cdot 2H_2O + 1.62\ K_2ZnxV_6O_{16} \cdot 1.5H_2O\ (2.14 > x > 0,\ 2.33 > y > 1.18) \qquad (8)$$
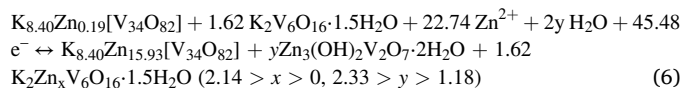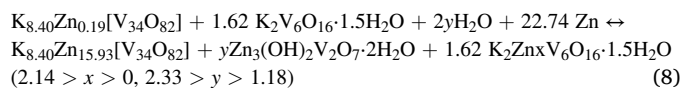
In the initial discharging process, Zn^{2+} ions insert into the KVO cathode to produce $K_{10}Zn_{6.73}[V_{34}O_{82}]$, and then the vast majority of Zn^{2+} ions are extracted to obtain $K_{8.40}Zn_{0.19}[V_{34}O_{82}]$ upon charging. The decreased K^+ ions are attributed to participating in an irreversible reaction in the voltage range of 1.4–1.5 V, which deliver a charge specific capacity of ~51 mAh g^{-1} at the current density of 0.05 A g^{-1}. During subsequent cycles, $K_{8.40}Zn_{0.19}[V_{34}O_{82}]$ and the irreversible product ($K_2V_6O_{16} \cdot 1.5H_2O$) serve as the host materials for reversible Zn^{2+} intercalation/deintercalation, which accompany with the reversible generation and consumption of $Zn_3(OH)_2V_2O_7 \cdot 2H_2O$. Due to the
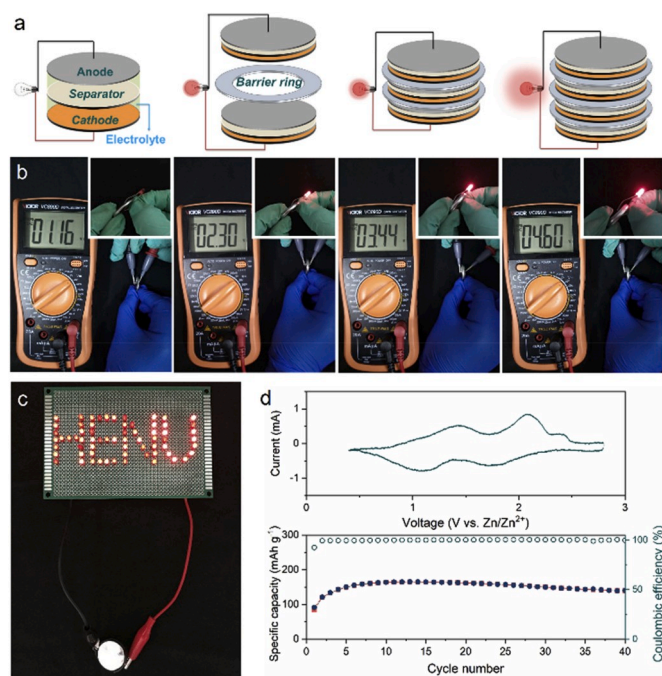
Fig. 6. (a) Structural illustration of the series-connected electrodes in a coin-type cell. (b) The tests of OCV and power LED lights. (c) LED array containing 66 bulbs powered by one cell ($E_{OCV} = 4.60$ V). (d) CV curve of the high OCV cell (2.3 V) in the voltage range of 0.4–2.8 V and its cyclic performance at a current density of 0.05 A g^{-1}.

narrow electrochemical stability window (1.23 V) of aqueous electrolyte, it is a significant challenge to acquire an aqueous battery with high open circuit voltage (OCV) [64]. Thus, various electrolyte stabilization strategies are considered as fundamental methods to expand the electrochemical stability window [1,65]. Herein, the Zn/KVO battery with high OCV (2.30–4.60 V) was assembled and integrated in a coin-type cell by the strategy of series-connected electrodes in order to reduce the mass of the inactive portion (Fig. 6a). As OCV rises, the brightness of LED lights powered by the single cell is boosted (Fig. 6b). Additionally, a single high OCV cell can light up sixty-six light-emitting diodes with a shape of "HENU" (Fig. 6c), illustrating the application potential of our high OCV batteries. Furthermore, the electrochemical test of the single cell with 2.30 V in the voltage range of 0.4–2.8 V exhibits the expanded operating voltage and favorable cycle reversibility by CV and GCD measurements (Fig. 6c–d, Fig. S15), which pave a feasible way for the practical application of aqueous ZIBs.

3. Conclusion and outlook

In summary, we firstly report a HNPC KVO with mixed-valence vanadium centers as a high-performance host material for zinc storage in aqueous ZIBs. Owing to the reversible redox activity and multidimensional hierarchical interconnected Zn^{2+} migration channels of mixed-valent KVO clusters, the resulting KVO cathode displays fast Zn^{2+} and electron diffusion kinetics and behaves as the high reversible capacity, excellent rate capability and impressive long-term cycle performance. Capitalizing on the KVO cathode, the quantitative redox reversibility of the KVO cluster and the Zn^{2+} intercalation/deintercalation mechanism have been investigated thoroughly, which clarify a reasonable and characteristic reaction process of electrodes during the first cycle and the subsequent cycles. Furthermore, a feasible optimizing strategy of the single cell structure to increase OCV and maintain electrochemical reversibility has been put forward. This finding firstly offers a reliable understanding of Zn^{2+} storage and POM's redox mechanism in a novel aqueous Zn/POM battery, which casts light on the design of more

advanced Zn^{2+} host materials and provide a promising direction for the POM application.

Declaration of competing interest

Our research interests are concentrated on design, fabrication and properties of advanced cathode materials in aqueous zinc-ion battery.

Appendix A. Supplementary data

Supplementary data to this article can be found online at https://doi.org/10.1016/j.nanoen.2020.104851.

References

[1] L. Suo, O. Borodin, T. Gao, M. Olguin, J. Ho, X. Fan, C. Luo, C. Wang, K. Xu, Science 350 (2015) 938–943.
[2] G. Fang, J. Zhou, A. Pan, S. Liang, ACS Energy Lett 3 (2018) 2480–2501.
[3] C. Kim, B.Y. Ahn, T.S. Wei, Y. Jo, S. Jeong, Y. Choi, I.D. Kim, J.A. Lewis, ACS Nano 12 (2018) 11838–11846.
[4] J. Huang, Z. Guo, Y. Ma, D. Bin, Y. Wang, Y. Xia, Small Methods 3 (2019) 1800272.
[5] Z. Wang, H. Li, Z. Tang, Z. Liu, Z. Ruan, L. Ma, Q. Yang, D. Wang, C. Zhi, Adv. Funct. Mater. 28 (2018) 1804560.
[6] M. Song, H. Tan, D. Chao, H.J. Fan, Adv. Funct. Mater. 28 (2018) 1802564.
[7] P. Yu, Y. Zeng, H. Zhang, M. Yu, Y. Tong, X. Lu, Small 15 (2019), e1804760.
[8] D. Kundu, S. Hosseini Vajargah, L. Wan, B. Adams, D. Prendergast, L.F. Nazar, Energy Environ. Sci. 11 (2018) 881–892.
[9] V. Verma, S. Kumar, W. Manalastas, R. Satish, M. Srinivasan, Adv. Sustainable Syst. 3 (2019) 1800111.
[10] A. Konarov, N. Voronina, J.H. Jo, Z. Bakenov, Y.-K. Sun, S.-T. Myung, ACS Energy Lett 3 (2018) 2620–2640.
[11] C. Xia, J. Guo, Y. Lei, H. Liang, C. Zhao, H.N. Alshareef, Adv. Mater. 30 (2018) 1705580.
[12] C. Liu, Z. Neale, J. Zheng, X. Jia, J. Huang, M. Yan, M. Tian, M. Wang, J. Yang, G. Cao, Energy Environ. Sci. 12 (2019) 2273–2285.
[13] Y. Yang, Y. Tang, S. Liang, Z. Wu, G. Fang, X. Cao, C. Wang, T. Lin, A. Pan, J. Zhou, Nano Energy 61 (2019) 617–625.
[14] G. Yang, T. Wei, C. Wang, ACS Appl. Mater. Interfaces 10 (2018) 35079–35089.
[15] D. Chao, C.R. Zhu, M. Song, P. Liang, X. Zhang, N.H. Tiep, H. Zhao, J. Wang, R. Wang, H. Zhang, H.J. Fan, Adv. Mater. 30 (2018), e1803181.
[16] F. Ming, H. Liang, Y. Lei, S. Kandambeth, M. Eddaoudi, H.N. Alshareef, ACS Energy Lett 3 (2018) 2602–2609.
[17] Y. Ji, L. Huang, J. Hu, C. Streb, Y.-F. Song, Energy Environ. Sci. 8 (2015) 776–789.
[18] J.J. Chen, J.C. Ye, X.G. Zhang, M.D. Symes, S.C. Fan, D.L. Long, M.S. Zheng, D. Y. Wu, L. Cronin, Q.F. Dong, Adv. Energy Mater. 8 (2018) 1701021.
[19] Y. Nishimoto, D. Yokogawa, H. Yoshikawa, K. Awaga, S. Irle, J. Am. Chem. Soc. 136 (2014) 9042–9052.
[20] T. Wei, M. Zhang, P. Wu, Y.-J. Tang, S.-L. Li, F.-C. Shen, X.-L. Wang, X.-P. Zhou, Y.-Q. Lan, Nano Energy 34 (2017) 205–214.
[21] J.C. Ye, J.J. Chen, R.M. Yuan, D.R. Deng, M.S. Zheng, L. Cronin, Q.F. Dong, J. Am. Chem. Soc. 140 (2018) 3134–3138.
[22] M. Genovese, K. Lian, Curr. Opin. Solid State Mater. Sci. 19 (2015) 126–137.
[23] Y. Hayashi, Coord. Chem. Rev. 255 (2011) 2270–2280.
[24] E. Kioseoglou, S. Petanidis, C. Gabriel, A. Salifoglou, Coord. Chem. Rev. 301 (2015) 87–105.
[25] Q. Li, L. Zhang, J. Dai, H. Tang, Q. Li, H. Xue, H. Pang, Chem. Eng. J. 351 (2018) 441–461.
[26] H. Wang, S. Hamanaka, Y. Nishimoto, S. Irle, T. Yokoyama, H. Yoshikawa, K. Awaga, J. Am. Chem. Soc. 134 (2012) 4918–4924.
[27] K.Y. Monakhov, W. Bensch, P. Kogerler, Chem. Soc. Rev. 44 (2015) 8443–8483.
[28] J.J. Chen, M.D. Symes, S.C. Fan, M.S. Zheng, H.N. Miras, Q.F. Dong, L. Cronin, Adv. Mater. 27 (2015) 4649–4654.
[29] F. Liu, Z. Chen, G. Fang, Z. Wang, Y. Cai, B. Tang, J. Zhou, S. Liang, Nano-Micro Lett. 11 (2019) 25.

[30] H. Song, C. Liu, C. Zhang, G. Cao, Nano Energy 22 (2016) 1–10.
[31] J. Shin, D.S. Choi, H.J. Lee, Y. Jung, J.W. Choi, Adv. Energy Mater. 9 (2019) 1900083.
[32] Y.-L. Ding, Y. Wen, C. Wu, P.A. van Aken, J. Maier, Y. Yu, Nano Lett. 15 (2015) 1388–1394.
[33] J. Lai, H. Zhu, X. Zhu, H. Koritala, Y. Wang, ACS Appl. Energy Mater. 2 (2019) 1988–1996.
[34] A. Müller, R. Rohlfing, J. Döring, M. Penk, Angew. Chem., Int. Ed. Engl. 30 (1991) 588–590.
[35] F. Wan, Y. Zhang, L. Zhang, D. Liu, C. Wang, L. Song, Z. Niu, J. Chen, Angew. Chem. Int. Ed. 58 (2019) 7062–7067.
[36] E.F. Wilson, H.N. Miras, M.H. Rosnes, L. Cronin, Angew. Chem. Int. Ed. 50 (2011) 3720–3724.
[37] A. Müller, M. Penk, R. Rohlfing, E. Krickemeyer, J. Döring, Angew. Chem., Int. Ed. Engl. 29 (1990) 926–927.
[38] L. Miao, W. Wang, K. Yuan, Y. Yang, A. Wang, Chem. Commun. 50 (2014) 13231–13234.
[39] Q. Pang, X. Liang, C.Y. Kwok, L.F. Nazar, Nat. Energy 1 (2016) 16132.
[40] Z.W. Seh, Y. Sun, Q. Zhang, Y. Cui, Chem. Soc. Rev. 45 (2016) 5605–5634.
[41] R. Fang, S. Zhao, Z. Sun, D.W. Wang, H.M. Cheng, F. Li, Adv. Mater. 29 (2017) 1606823.
[42] S. Zhang, Energies 5 (2012) 5190–5197.
[43] X.-B. Cheng, J.-Q. Huang, H.-J. Peng, J.-Q. Nie, X.-Y. Liu, Q. Zhang, F. Wei, J. Power Sources 253 (2014) 263–268.
[44] T. Wei, Q. Li, G. Yang, C. Wang, Electrochim. Acta 287 (2018) 60–67.
[45] N. Zhang, Y. Dong, M. Jia, X. Bian, Y. Wang, M. Qiu, J. Xu, Y. Liu, L. Jiao, F. Cheng, ACS Energy Lett 3 (2018) 1366–1372.
[46] P. Hu, T. Zhu, X. Wang, X. Wei, M. Yan, J. Li, W. Luo, W. Yang, W. Zhang, L. Zhou, Z. Zhou, L. Mai, Nano Lett. 18 (2018) 1758–1763.
[47] P. He, G. Zhang, X. Liao, M. Yan, X. Xu, Q. An, J. Liu, L. Mai, Adv. Energy Mater. 8 (2018) 1702463.
[48] D. Kundu, B.D. Adams, V. Duffort, S.H. Vajargah, L.F. Nazar, Nat. Energy 1 (2016) 16119.
[49] J. Ding, Z. Du, L. Gu, B. Li, L. Wang, S. Wang, Y. Gong, S. Yang, Adv. Mater. 30 (2018), e1800762.
[50] Y. Yang, Y. Tang, G. Fang, L. Shan, J. Guo, W. Zhang, C. Wang, L. Wang, J. Zhou, S. Liang, Energy Environ. Sci. 11 (2018) 3157–3162.
[51] S. Huang, C. Meng, M. Xiao, S. Ren, S. Wang, D. Han, L. Sun, Y. Meng, Nano Energy 61 (2019) 462–470.
[52] F. Wan, L. Zhang, X. Dai, X. Wang, Z. Niu, J. Chen, Nat. Commun. 9 (2018) 1656.
[53] J. Zhou, L. Shan, Z. Wu, X. Guo, G. Fang, S. Liang, Chem. Commun. 54 (2018) 4457–4460.
[54] J. Wang, J. Polleux, J. Lim, B. Dunn, J. Phys. Chem. C 111 (2007) 14925–14931.
[55] T. Brezesinski, J. Wang, S.H. Tolbert, B. Dunn, Nat. Mater. 9 (2010) 146–151.
[56] C. Xia, J. Guo, P. Li, X. Zhang, H.N. Alshareef, Angew. Chem. Int. Ed. 57 (2018) 3943–3948.
[57] V. Augustyn, P. Simonbc, B. Dunn, Energy Environ. Sci. 7 (2014) 1597–1614.
[58] D.T. Ngo, H.T. Le, C. Kim, J.-Y. Lee, J.G. Fisher, I.-D. Kim, C.-J. Park, Energy Environ. Sci. 8 (2015) 3577–3588.
[59] J. Zhao, J. Ren, Q. Liang, D. Yuan, S. Xi, C. Wu, W. Manalastas, J. Ma, W. Fang, Y. Zheng, C.-F. Du, M. Srinivasan, Q. Yan, Nano Energy 62 (2019) 94–102.
[60] N. Zhang, F. Cheng, Y. Liu, Q. Zhao, K. Lei, C. Chen, X. Liu, J. Chen, J. Am. Chem. Soc. 138 (2016) 12894–12901.
[61] B. Tang, G. Fang, J. Zhou, L. Wang, Y. Lei, C. Wang, T. Lin, Y. Tang, S. Liang, Nano Energy 51 (2018) 579–587.
[62] B. Tang, J. Zhou, G. Fang, F. Liu, C. Zhu, C. Wang, A. Pan, S. Liang, J. Mater. Chem. 7 (2019) 940–945.
[63] L. Chen, Y. Ruan, G. Zhang, Q. Wei, Y. Jiang, T. Xiong, P. He, W. Yang, M. Yan, Q. An, L. Mai, Chem. Mater. 31 (2019) 699–706.
[64] X. Chen, W. He, L.-X. Ding, S. Wang, H. Wang, Energy Environ. Sci. 12 (2019) 938–944.
[65] C. Yang, J. Chen, X. Ji, T.P. Pollard, X. Lu, C.J. Sun, S. Hou, Q. Liu, C. Liu, T. Qing, Y. Wang, O. Borodin, Y. Ren, K. Xu, C. Wang, Nature 569 (2019) 245–250.
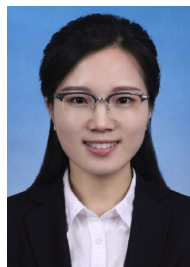
Yuanyuan Hu received her Ph.D. from Shandong University (China) under the supervision of Prof. Jingcheng Hao in 2018. Since then, she has been working in Henan University. Her research interests focus on the development of hydrogel materials and their applications in the field of electrochemical energy storage.
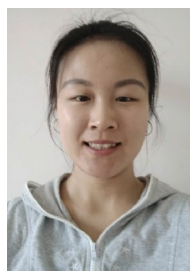
Lingyu Li was born in 1998, Xinjiang Province, China. She is studying at School of Chemistry and Chemical Engineering, Henan University, China. She is now doing her research on the development of novel polyoxometalates for energy conversion and storage under the supervision of Dr. Yang Kai and Prof. Junwei Zhao.
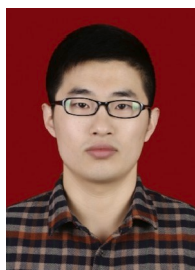
Lulu Cui was born in 1999, Henan Province, China. She is studying at School of Chemistry and Chemical Engineering, Henan University, China. Now she is doing research on the development of anode materials and flexible devices under the guidance of Dr. Kai Yang and Dr. Yuanyuan Hu.

Lei He received her B.S. degree from Tianjin University in 2011 and M.S. degree from Renmin University of China in 2014. Then she completed her Ph.D. at Nanyang Technological University in 2019 and worked as a research fellow there after graduation. She took her current position as an associate professor at the State Key Laboratory of Chemical Resource Engineering, Beijing University of Chemical Technology in the same year. Her research interests lie in highly interdisciplinary area at the interface of bioinorganic chemistry, biomimetic catalysis and electrochemical applications.

Kai Yang received his Ph.D. degree from Sun Yet-sen University (China) under the supervision of Prof. Yuezhong Meng in 2018. During the period of doctoral study, he paid more attention on the development of multifunctional separator for lithium-sulfur batteries. Then, he works at Henan University since 2018, and focuses on the design and application of cluster materials (e.g. Polyoxometalates, MOFs) for electrochemical energy storage & conversion such as zinc batteries and lithium batteries.

Shuanjin Wang received his PhD in polymer chemistry from Institute of Chemistry, CAS, China, in 2003. Since 2004, he has conducted postdoctoral research at McGill University, before moving to the Key Laboratory of Low-carbon Chemistry and Energy Conservation of Guangdong Province at Sun Yat-sen University in 2006 as an Associate Professor. He is currently a professor at Sun Yat-sen University, China. His research interests include polymer chemistry and new materials for energy conversion and storage. He has authored 120 publications in international journals.

Junwei Zhao obtained his BS (2002) and MS (2005) degrees from Henan University and received his PhD in 2008 from Fujian Institute of Research on the Structure of Matter, CAS. China. After that, he joined to Henan University and was promoted to a full professor of chemistry in 2014. In 2018, he was appointed as a distinguished professor of Henan Province. His current interests are concentrated on POM-based functional materials and their optical, electric, magnetic and biological properties. He has published over 140 papers in journals *Angew. Chem. Int. Ed., J. Am. Chem. Soc., Chem. Eur. J.* etc.

Yufei Song received his BS (1997) and PhD (2002) degrees from Shanxi University. After postdoc research in Leiden University, Max-Planck Institute of Bio-inorganic Chemistry and University of Glasgow, he joined Beijing University of Chemical Technology in 2008 (BUCT). He is currently a full professor of BUCT. His research directions focus on polyoxometalate-based molecular assemblies and multifunctional materials. He has published over 170 papers in *Nat. Commun., Nat. Protoc., Angew. Chem. Int. Ed., J. Am. Chem. Soc.* etc. He was awarded "Chang Jiang Scholars Program-Young Scholars, Ministry of Education" (2015), and "National Science Foundation for Distinguished Young Scholars of China" (2016).